processes

MDPI

Article

Efficient Geothermal Reservoir Simulation Using Deep Learning Surrogates and Multiscale Interpolation Techniques

Vaibhav V. Khedekar, Abdul R. A. N. Memon and Mayur Pal *

Department of Mathematical Modelling, Faculty of Mathematics and Natural Sciences, Kaunas University of Technology, 44249 Kaunas, Lithuania; vaibhav.khedekar@ktu.edu (V.V.K.); abdmem@ktu.lt (A.R.A.N.M.)
* Correspondence: mayur.pal@ktu.lt

Abstract

Accurate prediction of subsurface temperature distributions is essential for geothermal reservoir assessment, thermal performance evaluation, and decision support in reservoir management. However, repeated high-resolution numerical simulations are computationally expensive, particularly when multiple scenarios, heterogeneous petrophysical fields, and varying grid resolutions must be analyzed. This study presents a U-Net-based surrogate modeling framework for fast geothermal temperature field prediction on structured grids, coupled with interpolation strategies for handling unseen grid resolutions and intermediate time instances. Training and evaluation data are generated using the MATLAB Reservoir Simulation Toolbox (MRST) (24.1.0.2578822 (R2024a) Update 2) under multiple porosity–permeability realizations and at several grid resolutions (130×73, 67×37, 36×19, and 20×11) on a 2D grid. Data preprocessing and reshaping techniques are used to preserve spatial correspondence across resolutions. For fixed trained grids, the surrogate directly predicts temperature fields from porosity, permeability, and time inputs. For unseen grids, a grid interpolation strategy combines predictions from neighboring trained resolutions using weighted blending based on target grid cell count, followed by spatial resizing to the requested resolution. In addition, time interpolation is used to estimate temperature maps at intermediate time steps between predicted/simulated snapshots. The proposed framework enables rapid generation of temperature maps while maintaining spatial structure, making it suitable for efficient geothermal screening and multiscale scenario analysis.

Keywords: geothermal reservoir; surrogate modeling; U-Net; MRST; temperature prediction; multi-grid inference; grid interpolation; time interpolation

Academic Editor: Fabrizio Bezzo

Received: 14 March 2026
Revised: 7 April 2026
Accepted: 11 April 2026
Published: 14 April 2026

1. Introduction

Geothermal energy provides a scalable, low-carbon option for both electricity generation and direct heat supply. Its practical deployment, however, depends on the ability to predict subsurface temperature evolution under geological heterogeneity and operational uncertainty [1]. In geothermal reservoirs, heat transport is tightly coupled with fluid flow in porous media, such that permeability and porosity contrasts strongly influence advective and conductive heat transfer and, consequently, the spatial temperature response [2,3]. Besides permeability and porosity, other factors also impact heat transport in a geothermal reservoir, such as heterogeneity of fracture hydraulic conductivities in EGS reservoirs [4]. Robust spatio-temporal temperature forecasting is therefore central to geothermal prospect evaluation, system design, and long-term reservoir management [1].

From a modeling perspective, geothermal reservoir behavior is governed by coupled conservation laws for mass and energy in porous media, commonly expressed as PDE systems [2,3]. In practice, these equations are solved numerically using established discretization frameworks—finite differences, finite volumes, or finite elements—to achieve stable and physically consistent approximations of pressure and temperature fields [5–7]. Such methods underpin both research-grade and industrial simulation environments, including widely used geothermal simulators (e.g., TOUGH2) as well as commercial multi-physics platforms designed for field-scale studies [8,9]. Although simulation technology continues to progress—including recent developments in fast and flexible geothermal simulators—the computational cost of repeated forward simulations remains substantial when numerous geological realizations, uncertainty scenarios, multiple grid resolutions, and multiple time points must be evaluated [10].

To address some of these challenges, surrogate modeling approaches have been increasingly explored in geothermal reservoir engineering. Surrogate models, also known as reduced-order models or metamodels, aim to approximate the behavior of complex numerical simulators while significantly reducing computational cost. These models are typically constructed using machine learning techniques or statistical approximation methods trained on simulation data. For example, the researcher [11] developed deep learning-based surrogate models for geothermal reservoir production optimization, demonstrating that convolutional and recurrent neural networks can effectively emulate reservoir simulation outputs while enabling closed-loop optimization workflows. Similarly, author [12] proposed neural-network-based surrogate models capable of predicting pressure and temperature evolution in geothermal reservoirs, achieving high predictive accuracy with substantially reduced computational time.

Surrogate models have also been integrated with optimization algorithms to improve geothermal energy extraction strategies. The researcher [13] developed a surrogate-assisted evolutionary optimization framework for enhanced geothermal systems, enabling efficient identification of optimal injection and production strategies while reducing the number of required high-fidelity simulations. In addition, the author [14] introduced surrogate modeling techniques to represent the coupled dynamics of geothermal reservoirs and surface power plants, allowing rapid optimization of integrated geothermal energy systems.

Beyond machine learning approaches, statistical surrogate modeling techniques such as polynomial chaos expansions have also been applied to subsurface flow systems. The researcher [15] demonstrated the effectiveness of polynomial chaos-based surrogate models for approximating complex groundwater and geothermal flow simulations, enabling efficient uncertainty quantification and sensitivity analysis. Furthermore, recent studies have explored advanced machine learning approaches such as graph neural networks and deep learning frameworks to model complex fractured geothermal reservoirs and heterogeneous geological formations [16].

Another aspect of robust geothermal evaluation involves uncertainty management, in which multiple geological realizations are evaluated to support decision making. Although this approach provided physically consistent results, the repeated numerical simulations required significant computational time, especially when applied to regional-scale screening with multiple uncertainty scenarios. Hence, computational demanding tasks further highlight the need to develop a rapid surrogate-based workflow capable of reproducing physics-based simulation results with high accuracy while significantly reducing computational cost. By integrating a U-Net-based neural network surrogate with the regional screening framework, the proposed approach enables efficient prediction over the full spatial grid without the need to run simulations for every location. This capability makes

the method well suited for geothermal potential assessment under uncertainty, where fast evaluation of multiple scenarios is required for reliable regional-scale decision support.

Moreover, a regional screening workflow for geothermal potential assessment in the Cambrian reservoir system of western Lithuania was recently developed. In that work, archival well data were collected, cleaned, and combined into a consistent dataset, and key reservoir properties were spatially interpolated using ordinary kriging with uncertainty multipliers. The study area was represented on a structured grid of 25 × 30 cells covering about 6750 km^2, and standardized doublet simulations were performed to estimate thermal performance under low, medium, and high uncertainty scenarios (±10%). Physics-based simulations were carried out for selected grid locations and produced cumulative extracted energy indicators in the range of 10^5–10^7 MWh, which were used for comparison between cases.

Furthermore, a neural-network surrogate model was trained to reproduce the simulation results [17] which showed very high agreement with the numerical model (test $R^2 \approx 0.996$ and cross-validation $R^2 \approx 0.99$), allowing fast prediction for the remaining grid cells. These surrogate models were used to generate regional maps for identification of geothermal potential and provided a practical basis for planning further investigations.

Published work shows that, to reduce the cost of repeated numerical simulations, surrogate modeling has gained increasing attention, particularly with deep learning approaches that learn nonlinear mappings from inputs to outputs in an offline training stage [18]. CNNs are well suited for reservoir prediction tasks because they can directly learn spatial patterns from gridded representations of heterogeneous porous structures. Prior work has demonstrated CNN-based methods for permeability prediction and upscaling [19,20], as well as theory-guided neural networks for subsurface flow that improve learning and generalization by incorporating physical structure into the modeling process [21]. In addition, deep-learning-based porous-media upscaling and homogenization studies indicate that neural networks can accelerate modeling while preserving effective behaviors across scales [10]. Together, these findings support the use of deep learning as a complement to conventional simulation tools, provided that preprocessing and spatial indexing are handled consistently.

Using U-Net as a surrogate model, the workflow can reproduce physics-based simulation results with high accuracy and efficiently generate predictions for the full regional grid, making it well aligned with the objective of rapid geothermal potential screening under uncertainty [22]. Among CNN architectures, U-Net is particularly attractive because its encoder–decoder structure and skip connections preserve fine spatial detail while enabling multiscale feature learning [23]. Although originally proposed for biomedical segmentation, the U-Net design naturally suits reservoir-field regression, where temperature distributions often contain smooth plateaus combined with localized gradients near boundaries and heterogeneity transitions [1,18]. The multi-resolution feature hierarchy learned by U-Net therefore offers a practical backbone for temperature surrogate modeling when inputs are expressed as spatial property fields.

Despite these advantages, two practical barriers remain for deep-learning surrogate models in geothermal workflows. First, operational studies frequently require multiple grid resolutions to balance accuracy and runtime, while models trained at a single resolution often generalize poorly across grid sizes. Second, engineers commonly require predictions at intermediate time points and intermediate grid resolutions that were not explicitly simulated. Classical numerical analysis addresses such mismatches through interpolation, projection, and discretization-consistent transfer operations [5–7]; analogous procedures must be introduced carefully in data-driven approaches to avoid spatial misalignment and artificial artifacts. The workflow is shown in Figure 1.

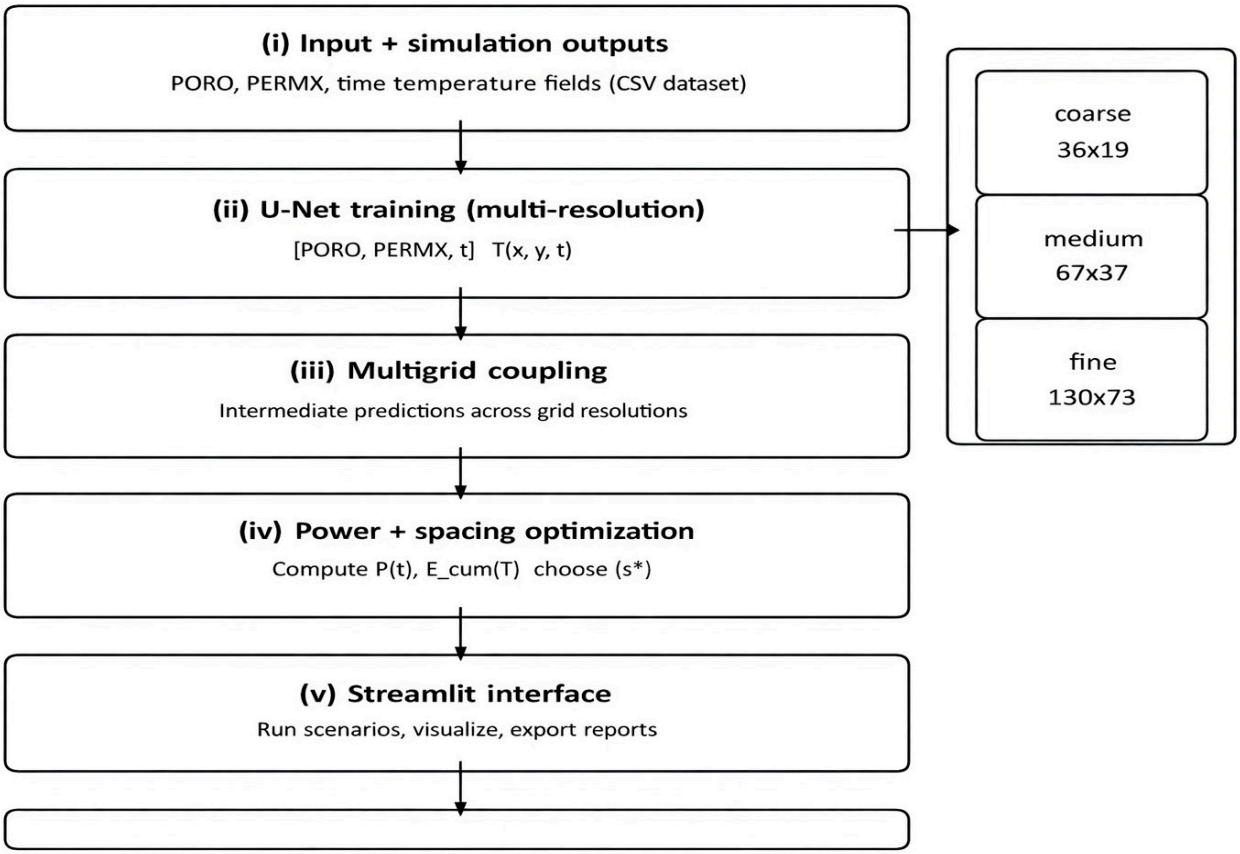

Figure 1. Software and data workflow for surrogate training, multigrid coupling, and geothermal prediction.

Geothermal assessments are also inherently site-specific, because thermal anomalies and structural controls vary regionally and can dominate reservoir behavior. In this study, the application setting is motivated by geothermal prospects in western Lithuania, where fault systems and spatially varying thermal conditions play a key role. Figure 2 summarizes the regional geothermal context and highlights the location of the selected study area used for dataset preparation. Among the candidate locations, the Vilkýčiai area is selected as a representative site for training-data generation and surrogate development, as it lies within the targeted geothermal trend indicated by the regional maps (Figure 2). This focus enables consistent sampling of porosity–permeability realizations and corresponding temperature responses while remaining aligned with the broader geological framework.

The main contributions of this study are summarized as follows:

1. U-Net-based geothermal temperature surrogates trained across multiple grid resolutions, enabling direct prediction on supported grids with consistent spatial representation [1,18].
2. A resolution-consistent preprocessing workflow that converts tabular (flattened) simulation outputs into grid-aligned tensor inputs compatible with discretization conventions [5–7].
3. Grid and time interpolation procedures that extend surrogate predictions to intermediate resolutions and intermediate times without requiring additional expensive simulations [8,9,24].
4. A site-grounded dataset preparation strategy based on the Lithuanian geothermal context and a focused study area (Vilkýčiai), as illustrated in Figure 2, ensuring coherent parameterization within the regional setting [25].

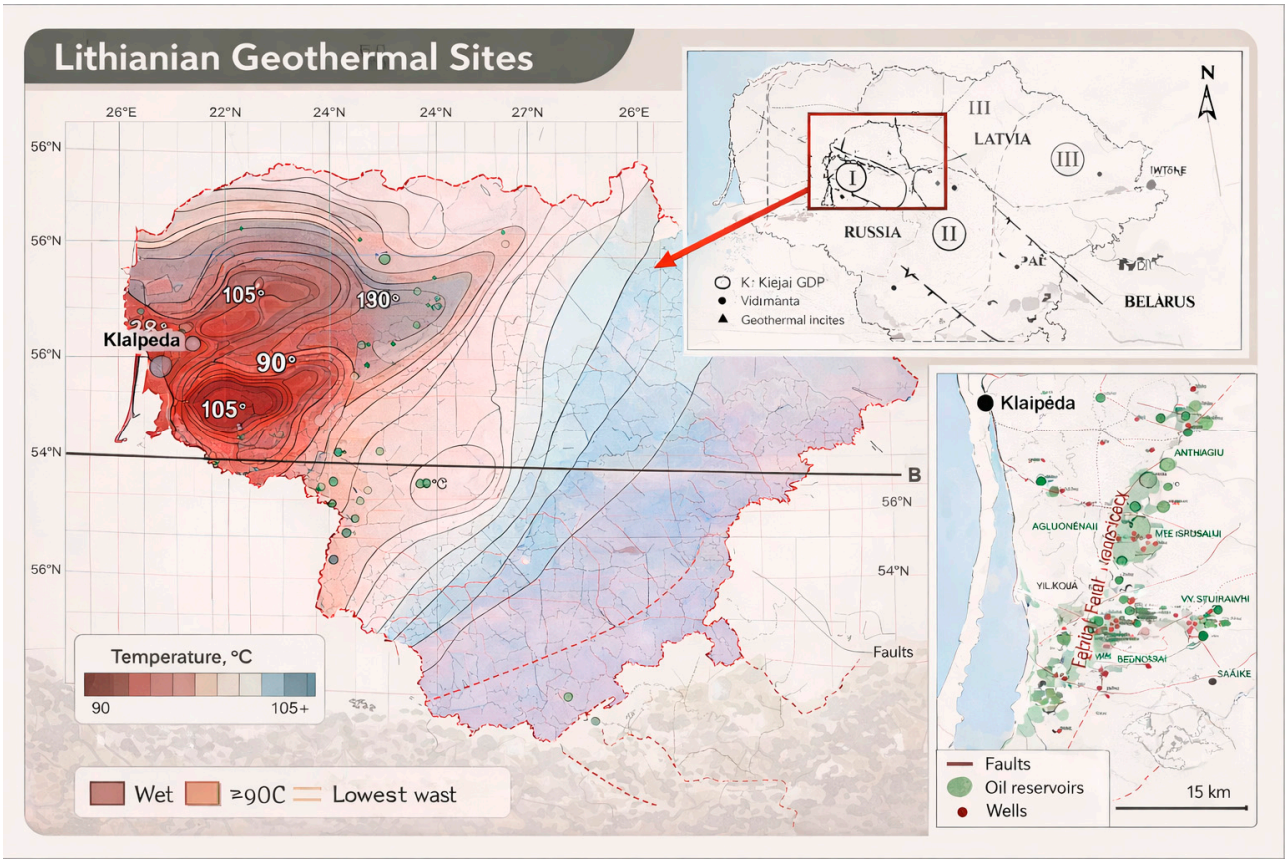

Figure 2. Lithuanian geothermal anomaly and geothermal sites in western Lithuania. The study area is shown in the red rectangle in the Baltic Sea region context. Green dots represent oil reservoirs in Cambrian reservoirs that were used for the initial screening.

2. Data Preparation

Figure 3 presents the workflow used for preparing the dataset that serves as the input for the MATLAB Reservoir Simulation Toolbox (MRST) simulator [26]. The dataset was designed to represent geothermal reservoir conditions within the Baltic Basin, with the Vilkyčiai field selected as the reference case for defining the reservoir property ranges. Although reservoir parameters were reviewed across multiple candidate sites within the basin, the porosity–permeability ranges reported for the Vilkyčiai field [27] were adopted to generate the simulation inputs used in this study.

The dataset was generated through repeated numerical simulations performed in MRST under heterogeneous reservoir property conditions [27,28]. The purpose of this process was to create paired input–output samples for surrogate model development. In this framework, the spatial distributions of porosity (ϕ) and permeability (k), together with time (t), serve as input variables, while the corresponding temperature field (T) represents the target output predicted by the surrogate model [28].

To construct the simulation inputs, representative ranges of key reservoir properties were first identified based on the geological characteristics of the target formation referred in Table 1. In particular, effective porosity and permeability ranges corresponding to the Vilkyčiai reservoir were considered. For each property, three representative levels were defined: low, medium, and high values. To improve the diversity of the dataset and achieve broader coverage of the parameter space, additional intermediate combinations of porosity and permeability were generated using linear interpolation between these end-member values.

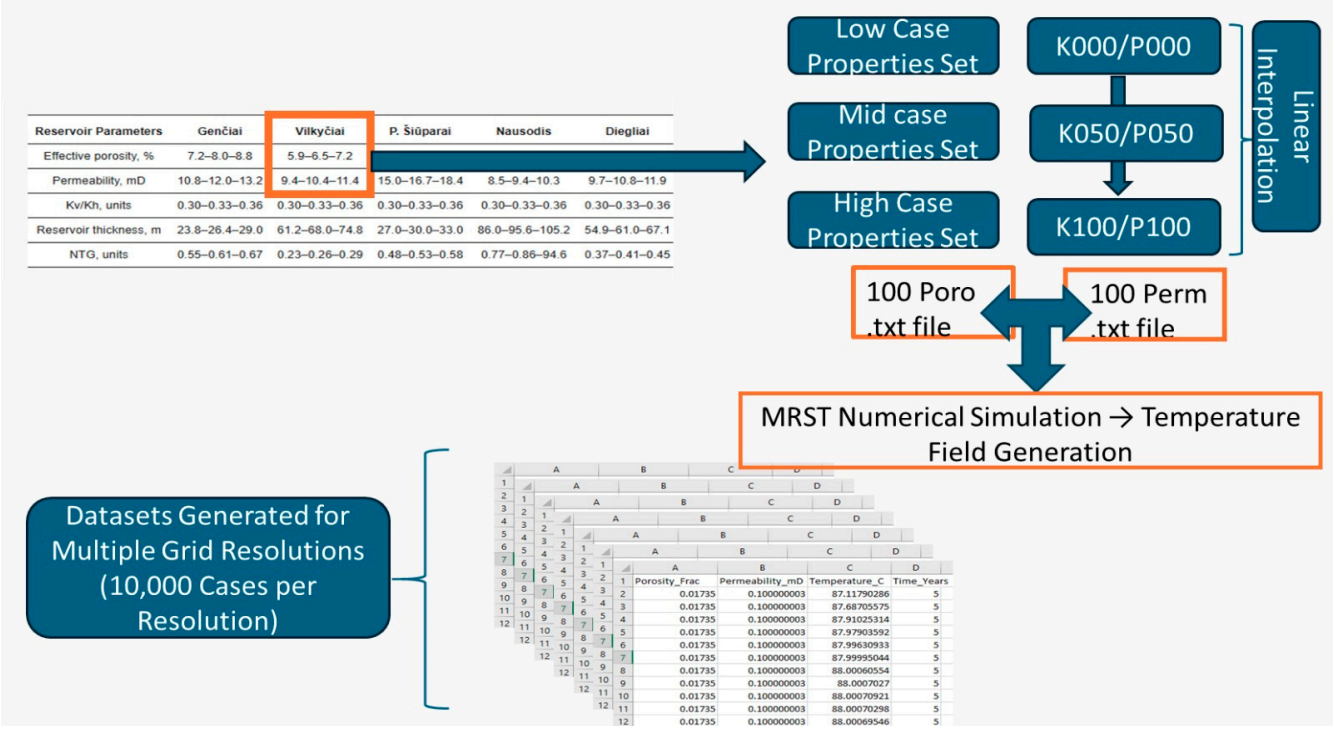

Figure 3. Illustrates the overall MRST-Matlab-based data generation and preparation workflow, including property-case construction, linear interpolation of porosity–permeability inputs, numerical simulation in MRST, and multi-resolution dataset creation.

Table 1. Characteristic of the MRST reservoir model.

Specifications	Parameters
Reservoir grid dimensions (Nx × Ny)	130 × 73, 67 × 37, 36 × 19, 20 × 11
Physical domain size	1500 × 200
Initial reservoir temperature (°C)	88
Thermal conductivity of rock (W/m.K)	2.4
Density of rock (Kg/m^3)	2700
Specific heat of rock (J/Kg.K)	1000
Re-injection temperature (°C)	40
Production temperature (°C)	88
Time period (years)	25

Using this approach, 100 spatial realizations were generated for each property and stored as text files representing different spatial distributions of porosity and permeability across the reservoir grid. By combining these realizations, a total of 10,000 input scenarios were created and used as inputs to the MRST simulations.

The numerical model represents a two-dimensional geothermal reservoir system where fluid flow and heat transport are simulated under gravity effects. The governing equations describing mass and energy conservation were solved to obtain the spatial and temporal evolution of temperature within the reservoir.

For each simulation case, the model produced spatial and temporal outputs describing reservoir behavior. The simulation results were recorded in terms of porosity (ϕ), permeability (k), temperature (T), and simulation time (t) at each grid cell. These outputs were subsequently organized into a structured dataset suitable for machine learning applications.

The resulting input–output pairs constitute the final dataset used for training and evaluating the surrogate model. A schematic overview of the entire data preparation and simulation workflow is presented in Figure 3.

Thus, for each generated porosity–permeability realization, MRST was used to run a numerical geothermal/thermal simulation and compute the corresponding temperature distribution on the grid. The resulting samples were stored in tabular form, where each row represents a grid cell (or indexed spatial location) and includes the local porosity, permeability, simulated temperature, and simulation time. This structure enables straightforward conversion to grid-based tensors for convolutional neural network training while preserving the spatial mapping of cell-wise properties.

To support multigrid surrogate modeling, the same data generation process was repeated for multiple structured grid resolutions. In this work, datasets were generated at several resolutions (e.g., 130×73, 67×37, 36×19, and 20×11), and a large number of cases were simulated for each resolution to ensure sufficient variability for training and interpolation-based inference. The use of multiple resolutions is essential for the proposed framework because it enables both direct prediction on trained grids and grid interpolation for unseen intermediate grid sizes.

3. Rationale for Selecting U-Net

The target output in this study is a 2D spatial temperature field over a geothermal reservoir grid, conditioned on cell-wise porosity, permeability, and simulation time. This is a structured grid-to-grid regression problem, where both local heterogeneity (e.g., near-well gradients and high/low permeability zones) and broader spatial thermal patterns must be preserved. For this reason, a U-Net (Figure 4)-based convolutional architecture was selected as the surrogate model.

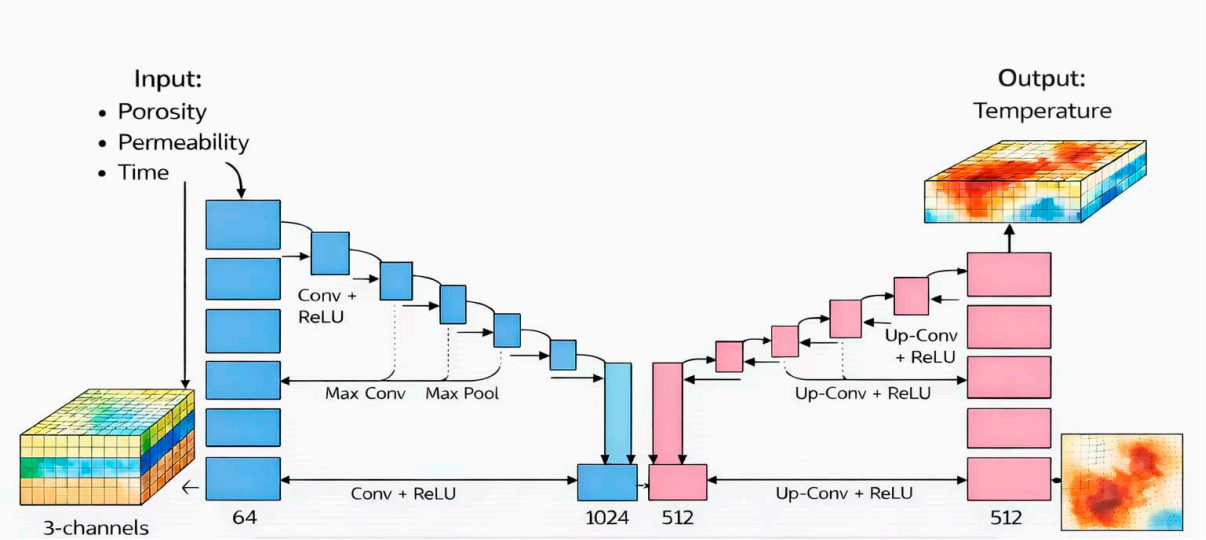

Figure 4. U-Net surrogate architecture used for geothermal temperature prediction. The white box represents Conv + ReLU layer, the green box represents Max Pooling, blue box represents UP-Conv + ReLU (Encoder) and pink box represents Up-Conv + ReLU (Decoder).

U-Net is well suited to this task for the following reasons:

5. Preservation of spatial structure.

The input and output are both arranged on structured grids. U-Net processes data as images/tensors, which allows the model to learn spatial correlations directly rather than treating each cell independently.

6. Multi-scale feature extraction.

The encoder path captures coarse/global thermal trends, while the decoder reconstructs fine-scale spatial details. This is important in geothermal fields, where temperature

distributions may contain both broad diffusion-driven patterns and localized variations caused by reservoir heterogeneity.

7. Skip connections for detail retention.

The skip connections in U-Net transfer high-resolution features from encoder layers to decoder layers. This helps preserve boundaries and local gradients that may otherwise be lost during down-sampling.

8. Compatibility with multigrid datasets.

Because the proposed framework uses multiple grid resolutions (e.g., 130 × 73, 67 × 37, 36 × 19, and 20 × 11), a convolutional architecture with flexible spatial handling is advantageous. The implemented U-Net variant includes size alignment during decoding (via interpolation where needed), enabling stable inference across trained grid sizes.

9. Computational efficiency for surrogate inference.

Once trained, the U-Net surrogate produces temperature maps much faster than repeated numerical simulations, making it suitable for rapid scenario screening and interpolation-based prediction workflows.

For these reasons, U-Net provides an effective balance between prediction accuracy, spatial fidelity, and computational speed for geothermal temperature surrogate modeling.

4. CSV to U-Net Input and Output Tensors

The simulator exports each scenario as a CSV table, with each row corresponding to one grid cell. For a grid of size (height (H) × width (W)), each time snapshot contains exactly (H · W) rows. The columns store the physical properties and the temperature at that cell. Although spatial coordinates (x, y) are not explicitly saved in the CSV, they are implicit because the simulator writes grid cells in a fixed, consistent order. Therefore, the flattened vectors of length (H.W) can be reshaped into 2D fields of size (H × W), representing spatial maps. After that, build matrices for input and output features.

It was an input feature including poro, perm, and time.

$$X_{\text{raw}} \in \mathbb{R}^{(H\cdot W)\times 3} = \begin{bmatrix} \phi_1 & k_{x,1} & t \\ \phi_2 & k_{x,2} & t \\ \vdots & \vdots & \vdots \\ \phi_{H\cdot W} & k_{x,H\cdot W} & t \end{bmatrix} \tag{1}$$

It was an output feature including temperature.

$$Y_{\text{raw}} \in \mathbb{R}^{(H\cdot W)\times 1} = \begin{bmatrix} T_1 \\ T_2 \\ \vdots \\ T_{H\cdot W} \end{bmatrix} \tag{2}$$

To improve numerical stability during training, both inputs and outputs are standardized using parameters fitted to the training set only:

$$X_{\text{sc}} = \text{Scaler}_X(X_{\text{raw}}) \, , Y_{\text{sc}} = \text{Scaler}_X(Y_{\text{raw}}) \tag{3}$$

Next, the flattened columns are reshaped into matrices of shape (H, W):

$$\begin{aligned} \phi(x,y) &= \text{reshape}(X_{\text{sc}}[:,1]) \in \mathbb{R}^{H\times W} \\ k(x,y) &= \text{reshape}(X_{\text{sc}}[:,2]) \in \mathbb{R}^{H\times W} \end{aligned} \tag{4}$$

Time value should be constant, but still needs to be reshaped into (H, W):

$$t(x,y) = t \cdot \mathbf{1} \in \mathbb{R}^{H \times W} \tag{5}$$

Similarly, temperature also needs to be reshaped:

$$Y(x,y,T) = \text{reshape}(y_{sc}) \in \mathbb{R}^{H \times W} \tag{6}$$

But the U-Net expects an image-like multi-channel tensor. We therefore stack three matrices (H, W). Input for the U-Net model is:

$$X(t) = [\Phi(x,y), K(x,y), t(x,y)] \in \mathbb{R}^{3 \times H \times W} \tag{7}$$

where $\Phi(x,y)$ and K(x, y) denote the spatial distribution of porosity and permeability, respectively, which is defined as a spatial uniform field.

$$t(x,y) = t \; \forall (x,y) \tag{8}$$

This formulation enables the network to learn the functional relationship between the petrophysical properties, time, and resulting temperature field.

$$T(x,y,t) = \alpha \; T\,(x,y,t_1) + (1-\alpha)\; T\,(x,y,t_2) \tag{9}$$

where the interpolation weight α is given by and performed element wise across all grid blocks:

$$\alpha = \frac{t_2 - t}{t_2 - t} \tag{10}$$

Output from U-Net model is:

$$\hat{Y}(T) = f_\theta(X(T)) \in \mathbb{R}^{1 \times H \times W} \tag{11}$$

Although the CSV stores one value per row, each time snapshot contains H · W rows (one per cell), and so reshaping reconstructs the spatial fields. Stacking ϕ (x, y), k (x, y), and a broadcast time map produces the three-channel tensor that the U-Net uses as input.

5. Training Setup

The U-Net surrogate model consists of the following hyper parameters which are elaborated in Table 2. A single baseline training configuration was adopted for all experiments to prioritize stability and reproducibility. Specifically, the network was optimized with Adam (learning rate 1×10^{-14}), and trained for 50 epochs using mini-batches of 16. Keeping hyperparameters fixed ensures that observed differences in model accuracy are primarily attributable to grid resolution and dataset characteristics rather than training-time re-tuning.

Table 2. U-Net surrogate model hyper parameters.

Parameters	Specifications
Learning rate	1×10^{-14}
Optimizer	Adam
Batch size	16
Epochs	50

Table 3 summarizes the test performance across the four trained resolutions. Among the models, the 36 × 19 grid achieved the highest R^2 value of 0.9420, while the 20 × 11 grid produced the lowest RMSE value of 2.2185. The 36 × 19 model also showed an RMSE of

2.3459, indicating a strong balance between prediction accuracy and goodness of fit. In contrast, the 130 × 73 model exhibited the lowest errors (RMSE = 2.132, MSE = 8.7459) and the lowest R^2 value of 0.8257.

Table 3. Test metrics for each trained grid resolution and mathematical definition of the metric.

Metric	20 × 11	36 × 19	67 × 37	130 × 73	Formula
RMSE	2.2185	2.3459	2.160	2.132	$RMSE = \sqrt{\left(\frac{1}{n}\right)\sum_{i=1}^{n}(y_i - \{y\}_i)^2}$
MAE	0.8364	0.9128	0.9917	0.5643	$MAE = \left(\frac{1}{n}\right)\sum_{i=1}^{n}(y_i - \hat{y}_i)$
MSE	4.9216	5.5035	8.2127	8.7459	$MSE = \left(\frac{1}{n}\right)\sum_{i=1}^{n}(Y_i - \{Y\}_i)^2$
R^2	0.9170	0.9420	0.9208	0.8257	$R^2 = 1 - \frac{\sum_{i=1}^{n}(Y_i - \hat{y})^2}{\sum_{i=1}^{n}(Y_i - \overline{Y})^2}$

6. Results

To demonstrate the behavior of the proposed surrogate framework under both trained-grid and unseen-grid conditions, two representative prediction cases are presented in Figures 5 and 6. The first case corresponds to a direct surrogate prediction on a grid resolution included during training (130 × 73), while the second case corresponds to an interpolated prediction on an intermediate grid resolution (78 × 45) not explicitly used during model training. The interpolated case additionally represents a prediction at a different time condition, illustrating the practical integration of both grid interpolation and time-based prediction/interpolation workflows in the proposed framework.

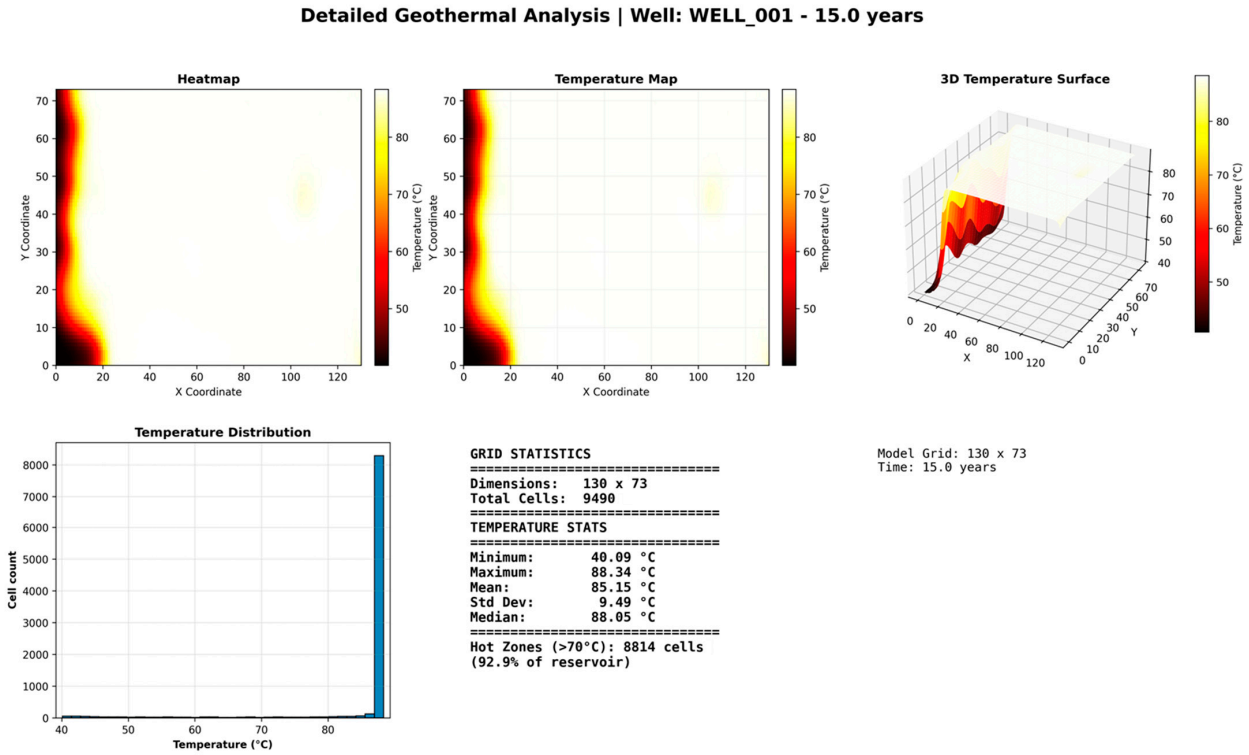

Figure 5. Detailed geothermal temperature prediction for WELL_001 at 15.0 years on the 130 × 73 grid (direct surrogate prediction on a trained resolution). Figure includes two 2D temperature maps, a 3D temperature surface view which is default using matplotlib, the temperature distribution histogram, and summary grid statistics.

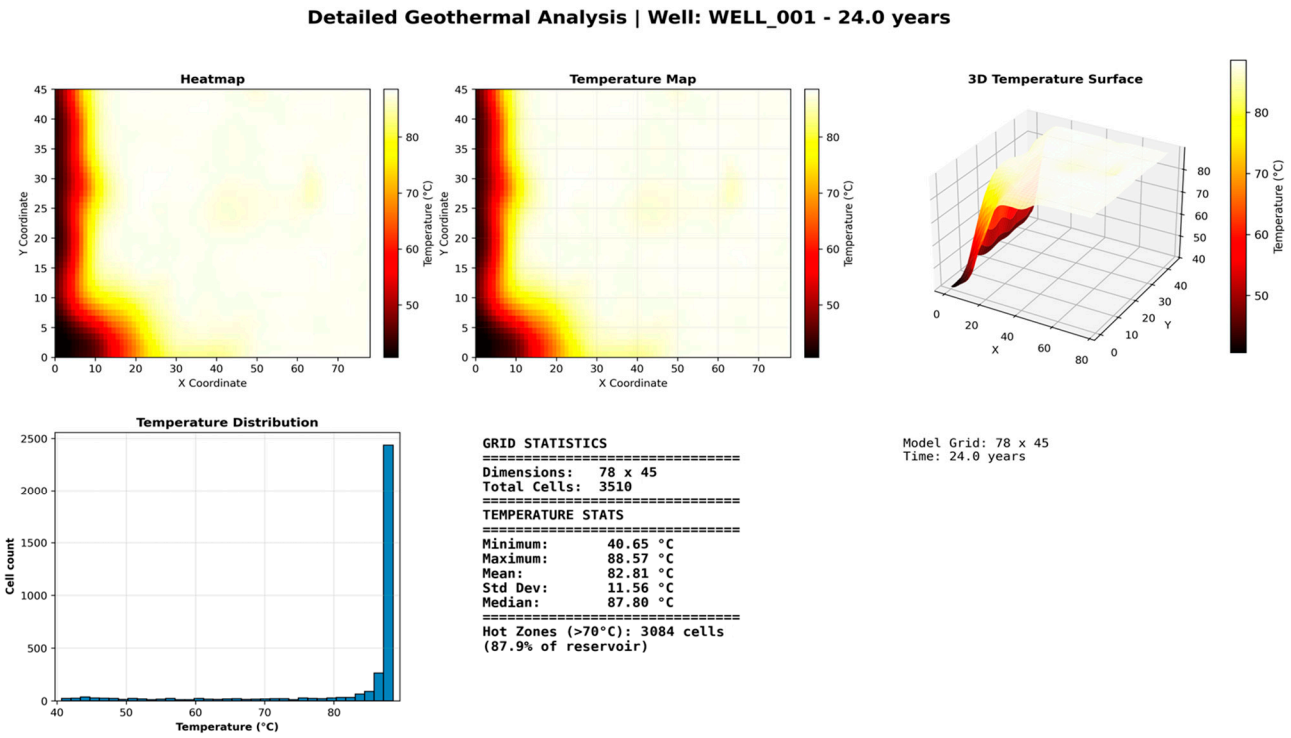

Figure 6. Detailed geothermal temperature prediction for WELL_001 at 24.0 years on the 78 × 45 grid (interpolated prediction on an unseen intermediate resolution). The result is obtained using the proposed multigrid interpolation framework; if applicable, the show case also reflects the use of time interpolation within the prediction workflow. Figure 6 includes two 2D temperature maps, a 3D temperature surface view which is default using matplotlib, the temperature distribution histogram, and summary grid statistics.

In both cases, the predicted temperature field preserves the expected geothermal pattern, with (i) a strong thermal gradient near the boundary region, (ii) smooth transition toward high-temperature zones in the interior, and (iii) physically plausible spatial continuity without obvious checkerboard or grid artifacts. The 2D heatmaps and 3D surfaces are consistent with one another, indicating stable surrogate behavior across visualization modes.

6.1. Direct Prediction on a Trained Grid (130 × 73, 15 Years)

Figure 5 shows the detailed geothermal analysis for WELL_001 at 15.0 years on the 130 × 73 grid, which is one of the resolutions used during training. Because this grid is directly supported by the trained U-Net model, no grid interpolation is required in this case. The prediction is therefore obtained through the standard forward pass of the surrogate model after preprocessing, normalization, and tensor reshaping.

The predicted temperature map shows a high-temperature dominant reservoir region with localized lower-temperature zones concentrated near the left boundary and lower-left corner. The corresponding statistical summary indicates a temperature range from 40.09 °C to 88.34 °C, with a mean of 85.15 °C and standard deviation of 9.49 °C. The high-temperature zone criterion (>70 °C) covers 92.9% of the reservoir cells, confirming that the predicted field is dominated by elevated thermal conditions at this time step.

The histogram further supports this observation, with a strong concentration of values near the upper temperature range, while the 3D surface representation highlights the sharp rise from the cooler boundary zone toward the interior plateau. Overall, this result demonstrates the surrogate model's ability to reproduce smooth and spatially coherent temperature distributions on trained resolutions.

6.2. Interpolated Prediction on an Unseen Intermediate Grid (78 × 45, 24 Years)

Figure 6 presents the detailed geothermal analysis for WELL_001 at 24.0 years on an intermediate grid (78 × 45), which is not one of the directly trained grid resolutions. In this case, the result is obtained using the proposed multigrid interpolation strategy, where predictions from neighboring trained grid models are resized to the target grid and combined through weighted interpolation. This enables temperature field estimation on unseen spatial resolutions while preserving spatial trends learned at known resolutions.

To enable predictions on unseen grid resolutions, a weighted blending strategy is employed using temperature fields predicted from the two nearest trained grid resolutions. Let N* denote the number of cells in the target grid, and N_1, N_2 denote the number of cells in the nearest lower and higher trained resolutions, respectively, such that $N_1 < N^* < N_2$. The corresponding predicted temperature fields are denoted as $T_1(x, y, t)$ and $T_2(x, y, t)$. These fields are first resized to the target grid resolution using spatial interpolation.

The blending weights are computed as

$$W_1 = \frac{N_2 - N^*}{N_2 - N_1} \; and \quad W_2 = \frac{N^* - N_1}{N_2 - N_1} \tag{12}$$

where $W_1 + W_2 = 1$.

The final temperature field at the target resolution is then obtained as:

$$T^*(x, y, t) = W_1 T_1 (x, y, t) + W_2 T_2(x, y, t) \tag{13}$$

This approach ensures a smooth interpolation across grid resolutions and enables resolution-flexible predictions without retraining the model.

The interpolated temperature field remains physically consistent with the direct-prediction case: a cooler boundary-driven region is visible near the left and lower-left edges, while the majority of the domain exhibits elevated temperatures. The interpolated result yields a temperature range of 40.65 °C to 88.57 °C, with a mean of 82.81 °C and standard deviation of 11.56 °C. Compared with the direct 130 × 73 case, the interpolated grid shows a slightly broader spread in temperatures, which is consistent with interpolation across resolutions and the different temporal conditions.

The hot-zone fraction (C) remains high at 87.9%, indicating that the interpolated prediction preserves the dominant thermal behavior while adapting the field to the target intermediate grid. The smooth 2D and 3D patterns suggest that the interpolation pipeline does not introduce severe discontinuities, supporting the suitability of the approach for resolution-flexible geothermal assessment.

If this 24.0-year case was produced using a time interpolation step (rather than a directly predicted time-specific model input), it also demonstrates that the framework can maintain spatial coherence when combining temporal interpolation with grid interpolation in a single workflow.

6.3. Error Convergence Across Grid Resolutions

Figure 7 shows how the surrogate model accuracy changes with grid resolution and time through its test set mean-squared error (NMSE) values. Surrogate model results are compared with numerical simulation results for corresponding grids and error is checked. The three grids used in this study appear on the horizontal axis with their corresponding NMSE values displayed on the vertical axis. The error rate decreases in a straight-line fashion when the grid resolution increases from 36 × 19 (coarse) to 67 × 37 (medium) and then to 130 × 73 (refined). The error rate of the coarse 36 × 19 model reaches its highest

point at 0.65 in normalized units, while the medium 67 × 37 model decreases the error to 0.20, and the refined 130 × 73 model achieves the lowest error rate below 0.06 for 25 years.

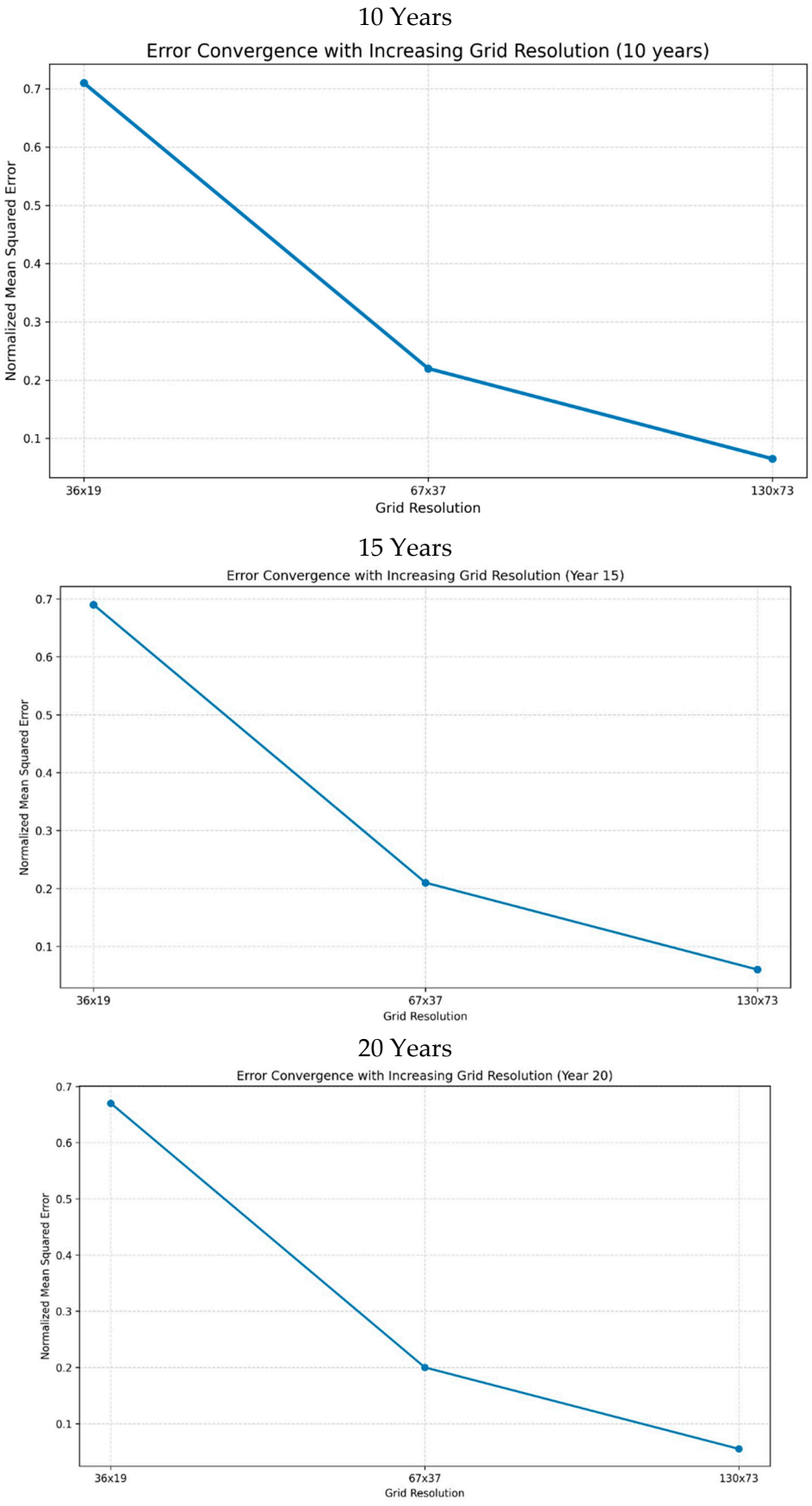

Figure 7. *Cont.*

Figure 7. Error convergence across grid resolutions for time steps of 10, 15, 20, and 25 years.

6.4. Comparison Between MRST Numerical Simulation and the U-Net Surrogate Model

Figure 8 compares the geothermal temperature fields produced by the high-fidelity MRST [28] numerical simulator and the proposed U-Net surrogate model and evaluates the corresponding prediction error as time progresses. Across the evaluated time horizon, the surrogate predictions preserve the main spatial structures of the simulated temperature field, including the dominant hot-region plateau and the colder zones influenced by boundary conditions and heterogeneous permeability–porosity distributions. This indicates that the surrogate captures the coupled heat–fluid-flow response in porous media and can reproduce physically consistent temperature patterns without performing a full numerical solve.

The error panel shows that prediction residuals are generally localized rather than spatially random. The largest deviations typically occur near sharp temperature gradients, such as boundary layers and transition regions where the temperature changes rapidly over short distances. In contrast, regions with smoother temperature variations exhibit smaller errors. This spatial error behavior is expected, because steep fronts are more sensitive to minor spatial shifts and resolution effects, while uniform plateaus are easier to approximate accurately.

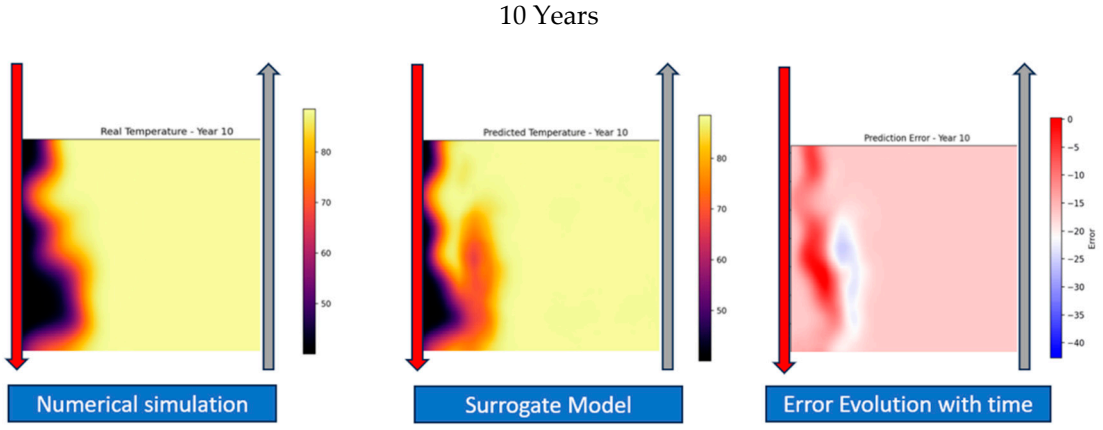

Figure 8. *Cont.*

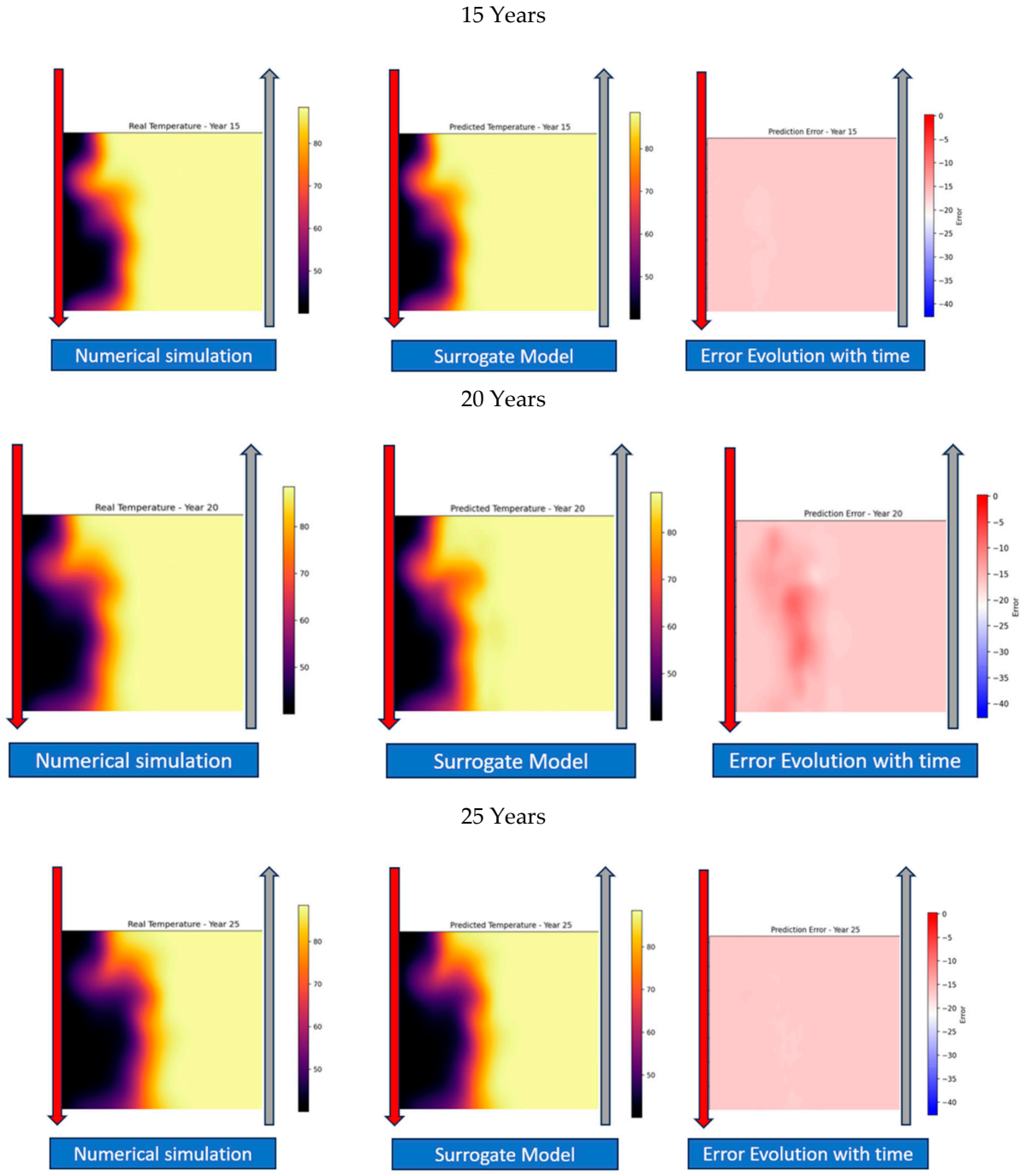

Figure 8. Comparison between MRST numerical simulation and the proposed U-Net surrogate model for geothermal temperature prediction, together with the corresponding error map for 10, 15, 20, and 25 years.

Figure 8 also proves that the largest prediction errors occur near sharp temperature gradients and boundary layers. In these regions, temperature changes very quickly over space. This usually happens due to strong interactions between heat conduction and fluid flow. From a modeling point of view, the U-Net uses convolution operations that look at local neighborhoods. This can smooth the results, especially in areas with steep temperature changes, and lead to local errors. In addition, the resolution of the training data and the use of discrete time snapshots may limit the model's ability to capture very fine details.

Overall, the predicted temperature fields remain physically reasonable. However, the model does not explicitly enforce physical laws such as energy conservation. Because

of this, small local errors can appear in regions where the physics is highly nonlinear. Moreover, adding physics-based constraints to the training process, such as including the heat transport equations in the loss function, could reduce these errors. This type of physics-informed approach is a promising direction for future work, especially for better capturing of sharp temperature fronts and boundary layer behavior.

7. Discussion

The proposed U-Net-based surrogate framework demonstrated effective multigrid temperature prediction capability across the four trained resolutions (20×11, 36×19, 67×37, and 130×73). The results indicate that the model can learn the nonlinear mapping from reservoir property fields (porosity and permeability) and time conditioning to spatial temperature distributions while preserving coherent thermal structures in the predicted maps. This behavior is consistent with the encoder–decoder design of U-Net, which combines local feature extraction with multiscale context aggregation and skip connections, making it suitable for grid-based geothermal temperature field regression.

A central contribution of this work is the resolution-consistent preprocessing and inference pipeline. The input data were originally stored in flattened tabular form but were systematically reshaped into grid tensors using a fixed cell-order convention (Fortran-order reshaping with controlled orientation handling). This step is critical because surrogate predictions can become spatially misleading when the flattening/reshaping order used during inference does not match the convention used during data generation and training. By preserving indexing consistency across all stages (MRST export, preprocessing, model input construction, and post-processing visualization), the framework ensures that the predicted temperature maps remain spatially aligned and interpretable.

The reported test metrics confirm good predictive performance across multiple grid resolutions, with some expected variation as grid complexity increases. These results suggest that the surrogate remains accurate on low-to-medium resolutions and still provides useful predictive capability on the highest tested resolution, although the error increases at 130×73 due to the greater spatial complexity and larger number of output cells. Such behavior is expected in dense-grid field prediction, where finer-resolution outputs contain more local variations and sharper gradients.

The multigrid design supports two practical inference modes. First, for grids that exactly match trained resolutions, the corresponding U-Net model is used directly for prediction. Second, for unseen intermediate grids, the framework uses an interpolation strategy based on predictions from neighboring trained grid models. Specifically, the input porosity and permeability fields (provided on the source grid) are resized to the neighboring trained grids, predictions are generated using each model, the predicted temperature fields are resized to the target grid, and a weighted combination is computed based on the relative cell-count position of the target grid between the two neighboring trained resolutions. This approach extends the surrogate to arbitrary intermediate grid sizes without requiring a dedicated retraining step for each new grid.

From a deployment perspective, this interpolation mechanism is a major advantage because geothermal screening workflows often require rapid comparisons across discretizations and time points. Instead of running a new MRST simulation or training a new surrogate for each mesh variant, the proposed method reuses a compact set of trained models and produces approximate intermediate-grid outputs with low computational cost. The interpolated results retain the dominant thermal gradients and high-temperature/low-temperature spatial regions, making them suitable for visualization, screening, and preliminary assessment. In addition, the same idea can be used for time interpolation, where

temperature fields predicted at discrete time points can be blended to estimate intermediate-time thermal states.

Despite these strengths, the current framework also has limitations. The interpolation process is based on geometric resizing and weighted blending and does not explicitly enforce physical conservation laws or thermodynamic constraints. As a result, interpolated outputs may smooth localized extrema or attenuate sharp thermal fronts, especially in highly heterogeneous reservoirs. Furthermore, the highest-resolution model (130 × 73) showed lower R^2 and higher error than the coarser grids, indicating that additional model capacity, training data diversity, or resolution-specific loss design may be beneficial for dense-grid prediction. Finally, the present study focuses on deterministic predictions; uncertainty quantification was not included, which limits direct risk-aware decision support.

8. Conclusions

This study developed a multigrid surrogate modeling framework for geothermal temperature prediction using a U-Net-based convolutional architecture trained on MRST-generated simulation data. The proposed workflow transforms flattened cell-wise porosity, permeability, and time information into structured grid tensors using a consistent preprocessing pipeline, enabling robust learning of spatial thermal patterns across multiple grid resolutions.

The framework was trained and evaluated on four grid resolutions (20 × 11, 36 × 19, 67 × 37, and 130 × 73), and the reported test metrics demonstrated strong predictive performance overall, with the best R^2 obtained on the 36 × 19 grid (R^2 = 0.9420), and stable performance also observed on 20 × 11 and 67 × 37. Although performance decreased on the highest-resolution grid (130 × 73), the surrogate still produced spatially coherent and practically useful temperature fields, confirming the feasibility of high-resolution inference with the current setup.

A key practical contribution of this work is the extension from direct fixed-grid prediction to interpolation-based prediction for unseen grid sizes. By combining predictions from neighboring trained resolutions using weighted interpolation after resizing, the framework can estimate temperature fields for intermediate grids without retraining additional models. The same interpolation principle also supports estimation at intermediate time points, improving flexibility for rapid scenario screening and reservoir monitoring workflows.

Overall, the proposed method provides a computationally efficient alternative to repeated full numerical simulation for geothermal temperature mapping while preserving spatial structure and interpretability. The combination of multigrid U-Net prediction, consistent tensor preparation, and grid/time interpolation makes the framework suitable for fast screening studies and iterative decision support. Future work will focus on improving high-resolution accuracy, incorporating uncertainty quantification, and introducing physics-guided constraints to further enhance generalizability and reliability.

Author Contributions: Conceptualization, M.P., A.R.A.N.M. and V.V.K.; methodology, V.V.K., A.R.A.N.M. and M.P.; software, V.V.K. and A.R.A.N.M.; validation, V.V.K.; formal analysis, V.V.K.; investigation, V.V.K., M.P. and A.R.A.N.M.; resources, V.V.K. and M.P.; data curation, V.V.K. and A.R.A.N.M.; writing—original draft preparation, V.V.K.; writing—review and editing, A.R.A.N.M., V.V.K. and M.P.; visualization, V.V.K., A.R.A.N.M. and M.P.; supervision, M.P.; project administration, M.P.; funding acquisition, M.P. All authors have read and agreed to the published version of the manuscript.

Funding: This work presented in this paper is partly supported by clean energy transition partnership funding for the Project GEOGUARD, project code S–CET–25–1 (SV3250308).

Data Availability Statement: The original contributions presented in this study are included in the article. Further inquiries can be directed to the corresponding author.

Acknowledgments: The authors gratefully acknowledge CETP for financial support of this work.

Conflicts of Interest: The authors declare no conflicts of interest.

References

1. Glassley, W.E. *Geothermal Energy: Renewable Energy and the Environment*, 2nd ed.; CRC Press: Boca Raton, FL, USA, 2014; pp. 9–10. [CrossRef]
2. Song, H. Fundamentals of fluid mechanics through porous media. In *Engineering Fluid Mechanics*; Springer: Singapore, 2018; pp. 171–197.
3. Bear, J. *Dynamics of Fluids in Porous Media*; Courier Corporation: New York, NY, USA, 2013; pp. 45–52. Available online: https://books.google.com/books/about/Dynamics_of_Fluids_in_Porous_Media.html?id=lurrmlFGhTEC (accessed on 13 April 2025).
4. Liu, S.; Ji, K.; Jin, M. Review of Techniques to Mitigate Thermal Breakthrough in Enhanced Geothermal Systems. *Preprints* **2025**, 2025050422. [CrossRef]
5. Smith, G.D. *Numerical Solution of Partial Differential Equations: Finite Difference Methods*, 3rd ed.; Oxford University Press: Oxford, UK, 1985; pp. 1–3. Available online: https://global.oup.com/academic/product/numerical-solution-of-partial-differential-equations-9780198596509 (accessed on 13 April 2025).
6. Versteeg, H.K.; Malalasekera, W. *An Introduction to Computational Fluid Dynamics: The Finite Volume Method*, 2nd ed.; Pearson Education: Harlow, UK, 2007; pp. 120–135. Available online: https://books.google.lt/books/about/An_Introduction_to_Computational_Fluid_D.html?id=NbYmEAAAQBAJ&redir_esc=y (accessed on 13 April 2025).
7. Zienkiewicz, O.C.; Taylor, R.L.; Zhu, J.Z. *The Finite Element Method: Its Basis and Fundamentals*, 6th ed.; Elsevier Butterworth-Heinemann: Oxford, UK, 2005; pp. 210–228. Available online: https://educate.elsevier.com/book/details/9780750664318 (accessed on 13 April 2025).
8. Pruess, K.; Oldenburg, C.M.; Moridis, G.J. *TOUGH2 User's Guide Version 2*; Lawrence Berkeley National Laboratory: Berkeley, CA, USA, 1999.
9. Klemetsdal, Ø.; Andersen, O.; Møyner, O. Fimbul.jl—Fast, Flexible, Robust, and Differentiable Geothermal Energy Simulation in Julia. In *Sixth EAGE Global Energy Transition Conference & Exhibition (GET 2025)*; European Association of Geoscientists & Engineers: Houten, The Netherlands, 2025; pp. 1–5. [CrossRef]
10. Software, R.F.-N. Technical Documentation, Accessed. Rock Flow Dynamics T-Navigator Official Website. 2025. Available online: https://rfdyn.com/ (accessed on 13 April 2025).
11. Wang, N.; Chang, H.; Kong, X.; Saar, M.O.; Zhang, D. Deep learning based closed-loop optimization of geothermal reservoir production. *arXiv* **2022**, arXiv:2204.08987. [CrossRef]
12. Li, F.; Guo, X.; Qi, X.; Feng, B.; Liu, J.; Xie, Y.; Gu, Y. A Surrogate Model-Based Optimization Approach for Geothermal Well-Doublet Placement Using a Regularized LSTM-CNN Model and Grey Wolf Optimizer. *Sustainability* **2025**, *17*, 266. [CrossRef]
13. Chen, G.; Jiao, J.J.; Jiang, C.; Luo, X. Surrogate-assisted level-based learning evolutionary search for geothermal heat extraction optimization. *Renew. Sustain. Energy Rev.* **2024**, *189*, 113860. [CrossRef]
14. Liu, Z.; Gudala, M.; Katterbauer, K.; Yan, B. Robust optimization of fully coupled geothermal reservoir and power plant system based on deep learning. *Energy Convers. Manag. X* **2026**, *30*, 101556. [CrossRef]
15. Rajabi, M.M.; Ataie-Ashtiani, B.; Simmons, C.T. Polynomial chaos expansions for uncertainty propagation and moment independent sensitivity analysis of seawater intrusion simulations. *J. Hydrol.* **2015**, *520*, 101–122. [CrossRef]
16. Ma, X.; Zhao, J.; Zhou, D.; Zhang, K.; Tian, Y. Deep Graph Learning-Based Surrogate Model for Inverse Modeling of Fractured Reservoirs. *Mathematics* **2024**, *12*, 754. [CrossRef]
17. Memon, A.R.A.N.; Pal, M. Advancing Geothermal Energy Recovery Through Reactive Transport Modelling and Horizontal Well Analysis: A Case Study of Lithuanian Reservoirs. *Processes* **2026**, *14*, 203. [CrossRef]
18. Makauskas, P.; Memon, A.R.; Pal, M. Geothermal Energy Potential Map in Western Lithuania: Data Integration, Kriging, Simulation, and Neural Network Prediction. *Processes* **2026**, *14*, 626. [CrossRef]
19. Ramos, E.M.; Borges, M.R.; Giraldi, G.A.; Schulze, B.; Bernardo, F. Prediction of permeability of porous media using optimized convolutional neural networks. *Comput. Geosci.* **2023**, *27*, 1–34. [CrossRef]
20. Ronneberger, O.; Fischer, P.; Brox, T. U-Net: Convolutional Networks for Biomedical Image Segmentation. In *Medical Image Computing and Computer-Assisted Intervention—MICCAI 2015*; Navab, N., Hornegger, J., Wells, W.M., Frangi, A.F., Eds.; Lecture Notes in Computer Science; Springer: Cham, Switzerland, 2015; Volume 9351, pp. 234–241. [CrossRef]
21. Wang, N.; Zhang, D.; Chang, H.; Li, H. Deep learning of subsurface flow via theory-guided neural network. *J. Hydrol.* **2020**, *584*, 124700. [CrossRef]

22. Pal, M.; Makauskas, P.; Malik, S. Upscaling porous media using neural networks: A deep learning approach to homogenization and averaging. *Processes* **2023**, *11*, 601. [CrossRef]
23. Memon, A.R.A.N.; Khedekar, V.V.; Pal, M. *Agentic AI-Driven Geothermal Reservoir Simulation and Optimization Using Surrogate Modelling for Rapid Site Screening*; SPE-232332-MS; Kaunas University of Technology: Kaunas, Lithuania, 2026; *Under Publication*.
24. Collignon, M.; Klemetsdal, Ø.S.; Møyner, O. Simulation of Geothermal Systems Using MRST. In *Advanced Modeling with the MATLAB Reservoir Simulation Toolbox*; Lie, K.-A., Møyner, O., Eds.; Cambridge University Press: Cambridge, UK, 2021; pp. 491–514.
25. Sayyafzadeh, M.; Guérillot, D. Rapid permeability upscaling using convolutional neural networks. In *ECMOR 2022*; European Association of Geoscientists & Engineers: Bunnik, The Netherlands, 2022; Volume 2022, No. 1, pp. 1–12. [CrossRef]
26. LeCun, Y.; Bengio, Y.; Hinton, G. Deep learning. *Nature* **2015**, *521*, 436–444. [CrossRef] [PubMed]
27. Makauskas, P.; Kaminskaite-Baranauskiene, I.; Rashid Abdul Nabi Memon, A.; Pal, M. Assessing geothermal energy production potential of Cambrian geothermal complexes in Lithuania. *Energie* **2024**, *17*, 1054. [CrossRef]
28. Lie, K.-A. *An Introduction to Reservoir Simulation Using MATLAB/GNU Octave: User Guide for the MATLAB Reservoir Simulation Toolbox (MRST)*; Cambridge University Press: Cambridge, UK, 2019.